Construction of Average STN Atlas using Image Registration and Reconstruction

Kanglin Chen, Stefan Heldmann, Jan Rühaak, and Marc Hallmann

Fraunhofer MEVIS, Lübeck, Germany
{kanglin.chen,stefan.heldmann,jan.ruehaak,marc.hallmann}@mevis.fraunhofer.de

Abstract. We present a new mathematical model to construct mean-like and median-like average STN (subthalamic nucleus) atlases based on image registration and reconstruction. The average STN atlases (ASAs) have average intensities and shapes of the STN regions. In particular, the construction of the ASAs does not depend on selecting a particular image as the template and is optimal to the datasets with respect to minimizing a cost functional.

For the application in deep brain stimulation, the ASAs can be used to accurately localize the target points of the STNs. For the validation of the outperformace of the ASAs, we compare them with anatomical atlases by executing the atlas to patient data registrations using clinical datasets.

Keywords: Deep brain stimulation, subthalamic nucleus, atlas construction, image registration, image reconstruction.

1 Introduction

Deep brain stimulation (DBS) for treating Parkinson's disease [Da1,PM1] has been rapidly developed since the 80s of the last century, and this treatment has been proved to be useful for reducing abnormal involuntary movements [PPA1]. DBS therapy involves the implantation of a brain pacemaker to subthalamic nucleus (STN) regions. Due to the small size of the STN and its individual variation in shape and spatial position, it is difficult to localize the target points of the STN regions for therapy planning and validation.

To suppress the individual variation is medical atlas a good ansatz. Medical atlas nowadays becomes an important tool in computational anatomy to study the variability between individuals and identify abnormal anatomic structures [GMT1,TM1]. Medical atlas can be mainly categorized into anatomical atlas by scanning the slides and reconstructing the volumes in the stereotaxic coordinates [PW1,KH1]; probabilistic atlas constructed in a Bayesian perspective [AF1,MSG1]; average anatomical atlas, which is normally constructed based on linear or non-linear image registration [JDJ1,BK1,GMT1].

In the research area of DBS, anatomical atlases are often used to localize the target point of the STN, denoted by tSTN. It can be roughly determined

with respected to the midcommissural point (MCP) [SW1], namely the average of anterior commissure (AC), posterior commissure (PC) of the so-called Talairach coordinates system [TT1]. In terms of the visible surrounding area and landmarks [PMM1], such as red nucleus, subthalamic zone, AC and PC, the tSTN can be marked half-automatically. The targeting process can be also done based on non-linear atlas to patient data registration using the atlas with manual marked tSTNs [DBC1,XBC1].

In this paper we will present a new mathematical modeling and algorithms for constructing the medical atlas in the target STN regions, namely the average STN atlas (ASA). The construction of the ASA is based on image registration and reconstruction. Our algorithms do not depend on selecting a particular image as the template and produce the atlas automatically. The ASA is optimal to the datasets with respect to minimizing a cost functional. In particular, using the L^2- and L^1-norm we are able to construct mean-like and median-like ASAs. The ASA unifies the individual features of the STN regions and keeps well the common structures and prominent edges of the target regions. Compared to anatomical atlas, using the ASA is able to make the atlas to patient data registration more robust and accurately, such that the localization of the tSTNs becomes more accurate.

This paper is organized as follows: In Section 2 we give a mathematical modeling of the ASA construction based on the L^2- and L^1-norm. Particularly, we introduce efficient algorithms to solve the L^2- and L^1-based image registration and reconstruction problems. In Section 3 we design an experiment for the validation of the ASAs. We compare them with anatomical atlases in terms of using the atlas to patient data registration based on clinical datasets.

2 Construction of Average STN Atlas

Since we are only interested in the left and right STN regions, the midpoints of these target regions could be fixated by a translation related to the MCP. After fixating the midpoints of the left and right STN bounding boxes, we create the boxes of size 30mm^3 around them. Figure 1 shows that the bounding boxes are large enough to contain the prominent edges of the STN regions.

After fixating the target regions, we can model formally the construction of the ASA based on them: Suppose that there exists a database consisting of N images $\mathcal{T}_1, \cdots, \mathcal{T}_N$ defined in domains $\Omega_1, \cdots, \Omega_N \subset \mathbb{R}^3$, which are the target STN regions. Let $\mathcal{T}_i$ have a zero extension, i.e. $\mathcal{T}_i(x) = 0$ for all $x \in \mathbb{R}^3 \setminus \Omega_i$ and $1 \leq i \leq N$. Due to the small size of the STN regions (cf. Figure 1) and computational efficiency, we assume affine registration as the underlying image registration for the ASA reconstruction. Therefore, we search for N affine deformation fields $(y_i)_{1 \leq i \leq N}$ with $y_i : \Omega_i \to \mathbb{R}^3$ and an ASA $\mathcal{R}$ defined in $\mathbb{R}^3$ by solving

$$\inf_{y_i, \mathcal{R}} \frac{1}{N} \sum_{i=1}^{N} \mathcal{D}(\mathcal{T}_i, \mathcal{R} \circ y_i), \tag{1}$$
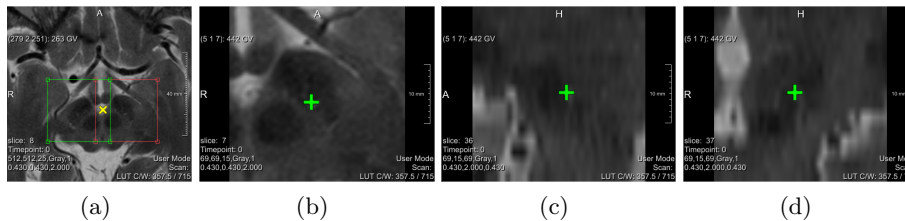
Fig. 1: (a) The axial view of the dataset with the left and right STN bounding boxes marked by red and green lines. The midpoints of the left and right bounding boxes are translated by the vectors $(11.5, 0.5, -6)$ and $(-11.5, 0.5, -6)$ related to the MCP marked by a yellow cross. In (b), (c) and (d) are showed the axial, sagittal and coronal views of the right STN bounding box in (a). The green cross marks the tSTN of the right STN region.

where $\mathcal{D}$ denotes the restricted L^p distance measure with $p \in \{1, 2\}$

$$\mathcal{D}(\mathcal{T}_i, \mathcal{R} \circ y_i) = \frac{1}{p} \int_{\mathbb{R}^3} \chi_{\Omega_i} \left| \mathcal{T}_i - \mathcal{R} \circ y_i \right|^p dx, \tag{2}$$

where χ_{Ω_i} denotes the indicator function of a target region Ω_i, in which χ_{Ω_i} equals to one, otherwise equals to zero. The motivation of using indicator functions lies on that every transformed ASA $\mathcal{R} \circ y_i$ should match $\mathcal{T}_i$ in the target region Ω_i as well as possible. Using (2) it is not simple to reconstruct $\mathcal{R}$, since it couples with unknown y_i. Applying the integral transformation we can decouple them, and equivalently we have

$$\mathcal{D}(\mathcal{T}_i, \mathcal{R} \circ y_i) = \frac{1}{p} \int_{\mathbb{R}^3} \chi_{y_i(\Omega_i)} \left| \mathcal{T}_i \circ y_i^{-1} - \mathcal{R} \right|^p |\det(\nabla y_i^{-1})| dx, \tag{3}$$

where $y_i(\Omega_i)$ is the transformed Ω_i by y_i and $\chi_{y_i(\Omega_i)}$ denotes the corresponding indicator function of domain $y_i(\Omega_i)$.

To solve (1) we utilize the alternating method [GOS1] described in Algorithm 1. In this algorithm we give an iterative framework based on solving two subproblems, namely image registration problem (4) and image reconstruction problem (5). For generating an initial guess $\mathcal{R}^0$, we set a point as the midpoint of $\mathcal{R}$ and translate the midpoints of $(\mathcal{T}_i)_{1 \leq i \leq N}$ to this point, then average them. With introduced distance measure (2) and its variation (3), we face to solve L^2- and L^1-based image registration and reconstruction problems. It will be detailedly explained in the following sections.

2.1 L^2-based Image Reconstruction

To compute an ASA in the sense of mean, we consider minimization problem (5) using restricted L^2-norm (3) with $p = 2$. Assume that $(y_i)_{1 \leq i \leq N}$ are fixed,

Algorithm 1

Initialize $\mathcal{R}^0$
for $k = 0, 1, \cdots\cdots$ **do**

$$y_i^{k+1} = \underset{y_i}{\operatorname{argmin}}\, \mathcal{D}(\mathcal{T}_i, \mathcal{R}^k \circ y_i), \quad i = 1, \cdots, N \tag{4}$$

$$\mathcal{R}^{k+1} = \underset{\mathcal{R}}{\operatorname{argmin}}\, \frac{1}{N} \sum_{i=1}^{N} \mathcal{D}(\mathcal{T}_i, \mathcal{R} \circ y_i^{k+1}) \tag{5}$$

end for

---

and consequently we can recover $\mathcal{R}$ by minimizing

$$\frac{1}{2N} \sum_{i=1}^{N} \int_{\mathbb{R}^3} \chi_{y_i(\Omega_i)}(x) \left(\mathcal{T}_i \circ y_i^{-1}(x) - \mathcal{R}(x)\right)^2 \left|\det(\nabla y_i^{-1}(x))\right| dx. \tag{6}$$

We compute the Gâteaux derivative of (6) with respect to $\mathcal{R}$ and derive that $\mathcal{R}$ has a closed formula

$$\mathcal{R}(x) = \frac{\sum\limits_{i=1}^{N} \chi_{y_i(\Omega_i)}(x) \mathcal{T}_i \circ y_i^{-1}(x) \left|\det(\nabla y_i^{-1}(x))\right|}{\sum\limits_{i=1}^{N} \chi_{y_i(\Omega_i)}(x) \left|\det(\nabla y_i^{-1}(x))\right|}. \tag{7}$$

In the case of affine registration, the deformation fields are invertible, and the Jacobi-determinants are not vanishing. If the denominator of (7) is zero at some point x, then $\chi_{y_i(\Omega_i)}(x) = 0$ for $i = 1, \cdots, N$. It means that x is not an element of the union of $(y_i(\Omega_i))_{1 \leq i \leq N}$, and we set $\mathcal{R}(x)$ to zero in this case. In the praxis, we define and discretize $\mathcal{R}$ in a domain, which is large enough to include the union of $(y_i(\Omega_i))_{1 \leq i \leq N}$.

2.2 L^1-based Image Reconstruction

Instead of the L^2-norm, using the L^1-norm we can compute the median-like ASA. Since the L^1-norm is non-smooth, we cannot expect to derive an explicit solution as in the case of L^2-minimization. However, we are able to develop an efficient algorithm to solve it. Assume that $(y_i)_{1 \leq i \leq N}$ are fixed, and using (3) with $p = 1$ we can recover $\mathcal{R}$ by minimizing

$$\frac{1}{N} \sum_{i=1}^{N} \int_{\mathbb{R}^3} \underbrace{\chi_{y_i(\Omega_i)}(x) \left|\det(\nabla y_i^{-1}(x))\right|}_{:= c_i(x)} \left|\mathcal{T}_i \circ y_i^{-1}(x) - \mathcal{R}(x)\right| dx.$$

Therefore, we can compute $\mathcal{R}(x)$ pointwise by minimizing

$$\sum_{i=1}^{N} c_i(x) \left|\mathcal{T}_i \circ y_i^{-1}(x) - \mathcal{R}(x)\right| \tag{8}$$

over $\mathcal{R}(x)$ in a domain, which is large enough to include the union of $(y_i(\Omega_i))_{1 \leq i \leq N}$. In the case of $c_i = 0$ for $i = 1, \cdots, N$, as we argued in the previous subsection that x is not an element of the union of $(y_i(\Omega_i))_{1 \leq i \leq N}$, and we set $\mathcal{R}(x) = 0$. Minimizing (8) is a so-called weighted median minimization problem [Gu1]. For simplicity we reformulate it in one dimensional case: Given N real numbers $x_1, \cdots, x_N$ and N non-negative weights $w_1, \cdots, w_N$, solve

$$\min_x f(x) = \min_x \sum_{i=1}^{N} w_i |x_i - x|.$$ (9)

The left and right derivatives of f are given by

$$f'_-(x) = \sum_{i:x_i<x} w_i - \sum_{i:x_i \geq x} w_i \text{ and } f'_+(x) = \sum_{i:x_i \leq x} w_i - \sum_{i:x_i>x} w_i.$$

Since f is convex and piecewise linear, the necessary and sufficient conditions for solving (9) are

$$f'_-(x) \leq 0 \text{ and } f'_+(x) \geq 0.$$

The number of points N is limited, so we test the N points to check which one actually fulfills the optimality conditions.

2.3 L^2- and L^1-based Image Registration

For affine image registration (4) using (2), we consider generally for given $\mathcal{T}$ defined in $\Omega_{\mathcal{T}}$ and $\mathcal{R}$ defined in $\Omega_{\mathcal{R}}$ the following minimization problem

$$\min_y \frac{1}{p} \int_{\Omega_{\mathcal{T}}} |\mathcal{T} - \mathcal{R} \circ y|^p \, dx.$$ (10)

In the case of $p = 2$, after discretization this is a standard affine registration using the sum of squared differences (SSD). We apply the Gauss-Newton algorithm to obtain the solution [Mo1]. In the case of $p = 1$, we present this problem as the affine registration using the sum of absolute differences (SAD). Since it is not quadratic and non-smooth, it could not be solved in the same fashion as the SSD. To handle such problem, we apply the non-linear primal-dual hybrid gradient method [Va1]: We discretize $\mathcal{T}$ and $\mathcal{R}$ on their domains with n grid points and denote them by T and R, respectively. Then, in the discrete setting we can reformulate (10) as the saddle point problem

$$\min_y \max_v v^t(T - R \circ y) - \delta_V(v),$$

where $v \in \mathbb{R}^n$ is the dual variable and the convex set V is given by

$$V = \{v \in \mathbb{R}^n : \|v\|_\infty \leq 1\}.$$

The projection function δ_V is equal to 0 if $v \in V$, otherwise equal to $+\infty$. To solve the saddle point problem, we apply the exact NL-PDHGM proposed in [Va1].

3 Evaluation

In this section we will introduce clinical datasets and design an experiment for validating the L^2- and L^1-ASA constructed by Algorithm 1. As mentioned in Section 1, the ASAs have the application of tSTN targeting, and it involves an affine image registration from the ASAs to patient data. For the validation of the ASAs we will compare them with anatomical atlases, by computing the affine registrations to a patient database. To get more robust affine registration results, we utilize the normalized gradient field (NGF) distance measure mentioned in [Mo1], since the NGF only relies on edge informations.

As in Figure 1 illustrated, the T2 weighted MRI images are used for the ASA construction. In each image the AC, PC and interhemispheral point (IH) are annotated, which build the Talairach coordinates. Additionally, the left and right tSTNs are annotated by 3 experts. We take the mean of 3 annotations as the tSTNs for one dataset. The total amount of T2 weighed images is 39, among them there are 19 1.5-Tesla images, 18 3-Tesla images and 2 7-Tesla images.

3.1 Experiments

We use 8 1.5-Tesla and 9 3-Tesla images to construct the L^2- and L^1-ASA (see Figure 2) by introduced algorithms. After construction we get the point clusters of the ACs, PCs, IHs and tSTNs for the left and right STN regions. Then, we compute the median of every cluster as the AC, PC, IH and tSTN of the ASA. As showed in Figure 2 we stitch the left and right ASAs together based on the Talairach coordinates of the left side .
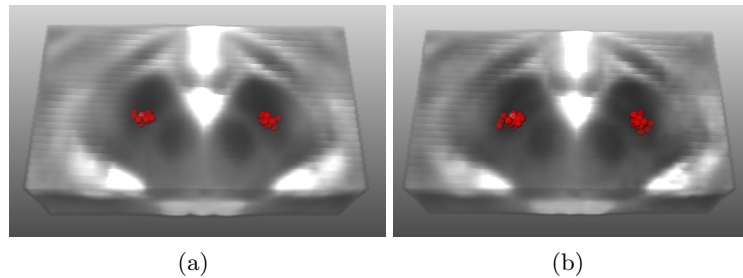

(a) (b)

Fig. 2: The left and right L^2-ASA and L^1-ASA in the bounding boxes are merged together. The red cluster points are the transformed tSTNs from the datasets. (a) The L^2-ASA. (b) The L^1-ASA.

We apply 17 datasets used for the ASA construction as the anatomical atlases again, and consequently we regard the rest 20 1.5-Tesla and 3-Tesla images as the patient database. For each ASA and anatomical atlas, we pre-align it to every

image in the patient database based on a rigid transformation using their AC-PC vectors and MCP-IH vectors. After the pre-alignment we compute the affine registration from the ASA or anatomical atlas to every image in the patient database for the left and right STN regions, respectively. Totally, we have 40 registrations for each ASA and anatomical atlas. It is also interesting to compare the ASAs with high quality 7-Tesla images, so we regard two 7-Tesla images as the anatomical atlases and register them to the patient database in the same way. After computing the ASA or anatomical atlas to patient data registrations, we compute the tSTN distances between the transformed ASA or anatomical atlas and every image in the patient database.

3.2 Results

We summarize the validation results with the introduced experiment. In Table 1 we list the results of the ASAs and anatomical atlases to patient data registrations. For anatomical atlases we list the results of the worst and best cases of 1.5-Tesla, 3-Tesla and 7-Tesla. We denote them XT_W and XT_B, where XT denotes the strength of magnetic field. The worst case and the best case of anatomical atlases are so classified that among the anatomical atlases with same strength of magnetic fields, the one gives the worst or best median results of tSTN distances. In Figure 3 we visualize the tSTN distances of the ASAs and anatomical atlases in a boxplot.

	L^2-ASA	L^1-ASA	1.5T_W	1.5T_B	3T_W	3T_B	7T_W	7T_B
median	0.91	0.82	1.89	0.98	1.95	1.24	1.45	1.17
mean	1.02	0.88	2.01	1.13	2.29	1.25	1.61	1.17
std	0.47	0.34	0.83	0.53	1.18	0.54	0.78	0.47

Table 1: Statistical evaluation of the ASA to patient data registrations and anatomical atlases to patient data registrations in mm.

Observing the tables and plots, we can identify that the ASAs and anatomical atlases give reasonable results, since the pre-alignment based on the AC, PC and IH produces a reliable initial transformation. Among them the ASAs give best and most stable results comparing to anatomical atlases. It is obvious to see that in Figure 3 the ASAs, especially the L^1-ASA produces fewer outliers than the others, no outliers larger than 1.5mm.

Comparing the L^2- and L^1-ASA, the L^1-ASA produces more reliable results with smaller variations. To explain this phenomenon, we observe the ASAs visualized in Figure 2 and determine that the L^1-ASA gives more local structures due to the median property of the L^1-norm. Such local structures make the registrations based on the NGF more robust.

Totally, we can conclude that the L^2-, and especially the L^1-ASA is suitable for accurate tSTN targeting due to the small tSTN distances.
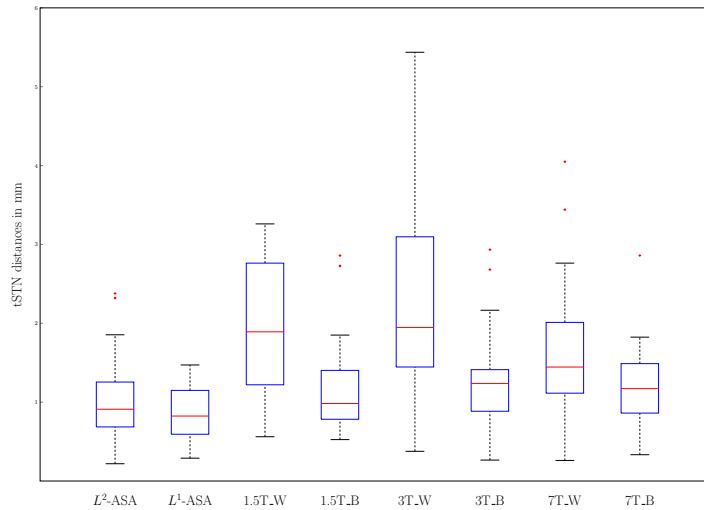
Fig. 3: The corresponding boxplot of Table 1.

4 Conclusion

We introduced a new mathematical modeling for the construction of the ASAs based on the L^2- and L^1-norm. The alternating algorithm involves of solving the L^2- and L^1-based image registration and reconstruction problems. We designed an experiment to compare the ASAs with anatomical atlases with the application of tSTN targeting using clinical datasets. Based on the experiment results, we can conclude that the ASAs work more accurately in the tSTN targeting than anatomical atlases due to the small tSTN distance.

References

[AF1] Ashburner, J., Friston, K.J.: Computing average shaped tissue probability templates. NeuroImage, 45(2), 333–341 (2008).

[BK1] Beg, M.F., Khan, A.: Computing an average anatomical atlas using LDDMM and geodesic shooting. ISBI, 1116–1119 (2006).

[Da1] Davie, C.A.: A review of Parkinson's disease. British Medical Bulleti, 86(1), 109–127 (2008).

[DBC1] Duay, V., Bresson, X., Castro, J.S., Pollo, C., Cuadra, M.B., Thiran, J.P.: An Active Contour-Based Atlas Registration Model Applied to Automatic Subthalamic Nucleus Targeting on MRI: Method and Validation. MICCAI 2, 5242, 980–988 (2008).

[GMT1] Guimond, A., Meunier, J., Thirion, J.P.: Average Brain Models: A Convergence Study. Computer Vision and Image Understanding, 77(2), 192–210 (2000).

[GOS1] Goldstein, T., O'Donoghue, B., Setzer, S.: Fast alternating direction optimization methods. CAM report 12–35, UCLA (2012).

[Gu1] Gurwitz, C.: Weighted median algorithms for L^1 approximation. BIT Numerical Mathematics, 30(2), 301–310 (1990).

[HMM1] Hamid, N.A., Mitchell, R.D., Mocroft, P., Westby, G.W., Milner, J., Pall, H.: Targeting the subthalamic nucleus for deep brain stimulation: technical approach and fusion of pre- and postoperative MR images to define accuracy of lead placement. J Neurol Neurosurg Psychiatry, 76(3), 409–414 (2005).

[GMT1] Guimond, A., Meunier, J., Thirion J.P.: Average brain models: a convergence study. Computer Vision and Image Understanding, 77(2), 192–210 (2000).

[JDJ1] Joshi, S., Davis, B., Jomier, M., Gerig, G.: Unbiased diffeomorphic atlas construction for computational anatomy. NeuroImage, 23, 151–160 (2004).

[KH1] Karten, H.J., Hodos, W.: A Stereotaxic Atlas of the Brain of the Pigeon. John Hopkins Press, 1967.

[Mo1] Modersitzki, J.: FAIR: Flexible Algorithms for Image Registration. SIAM, 2009.

[MSG1] Murgasova, M., Srinivasan, L., Gousias, I.S., Aljabar, P., Hajnal, J.V., Edwards, A.D., Rueckert, D.: Construction of a dynamic 4D probabilistic atlas for the developing brain. ISBI, 952–955 (2010).

[PM1] Perlmutter, J.S., Mink, J.W.: Deep brain stimulation. Annual Review of Neuroscience, 29(1), 229–257 (2006).

[PMM1] Pollo, C., Meuli, R., Maeder, P., Vingerhoets, F., Ghika, J., Villemure, J.G.: Subthalamic nucleus deep brain stimulation for Parkinson's disease: magnetic resonance imaging targeting using visible anatomical landmarks. Stereotact Funct Neurosurg, 80(1-4), 76–81 (2003).

[PPA1] Peppe, A., Pierantozzi, M., Altibrandi, M.G., Giacomini, P., Stefani, A., Bassi, A., Mazzone, P., Bernardi, G., Stanzione, P.: Bilateral GPi DBS is useful to reduce abnormal involuntary movements in advanced Parkinson's disease patients, but its action is related to modality and site of stimulation. European Journal of Neurology, 8, 579–586 (2001).

[PW1] Paxinos, G., Watson, C.: The Rat Brain in Stereotaxic Coordinates. Academic Press, 1998.

[SW1] Schaltenbrand, G., Wahren, W.: Atlas for Stereotaxy of the Human Brain. Thieme, 1977.

[TM1] Toga, A.W., Mazziotta, J.C.: Brain Mapping: The Methods. Academic Press, 2002.

[TT1] Talairach, J., Tournoux, P.: Co-Planar Stereotaxic Atlas of the Human Brain. Thieme, 1988.

[Va1] Valkonen, T.: A primal-dual hybrid gradient method for nonlinear operators with applications to MRI. Inverse Problems, 30(5), 055012 (2014).

[XBC1] Xiao, Y., Bailey, L., Chakravarty, M.M., Beriault, S., Sadikot, A.F., Pike, G.B., Collins, D.L.: Atlas-Based Segmentation of the Subthalamic Nucleus, Red Nucleus, and Substantia Nigra for Deep Brain Stimulation by Incorporating Multiple MRI Contrasts. IPCAI, LNAI 7330, 135–145 (2012).